Experimental and mathematical modelling of corrosion behaviour of CMAS coated oxide/oxide CMCs

Ramachandran, K., Chaffey, B., Zuccarini, C., Bear, J. C. & Jayaseelan, D. D

DOI 10.1016/j.ceramint.2022.09.294
ISSN 0272-8842
ESSN 1873-3956

Publisher: Elsevier

Ceramics International 49 (2023) 4213–4221

Contents lists available at ScienceDirect

Ceramics International

journal homepage: www.elsevier.com/locate/ceramint

Experimental and mathematical modelling of corrosion behaviour of CMAS coated oxide/oxide CMCs

Karthikeyan Ramachandran [a,*], Brace Chaffey [a], Carmine Zuccarini [a], Joseph C. Bear [b], Doni Daniel Jayaseelan [a,**]

[a] Department of Aerospace and Aircraft Engineering, Kingston University, Roehampton Vale Campus, London, SW15 3DW, United Kingdom
[b] Department of Chemical and Pharmaceutical Sciences, Kingston University, Penrhyn Road, Kingston upon Thames, KT1 2EE, United Kingdom

ARTICLE INFO

Keywords:
Oxide-oxide CMCs
Corrosion behaviour
CMAS
Fracture toughness and diffusion model

ABSTRACT

CMAS corrosion of turbine blades is a crucial failure in turbine engines and their components. In this study, oxide/oxide CMCs (AS-N610), which are candidates for gas turbine (GT) applications, are investigated for its corrosion behaviour at different temperatures and time in presence of CMAS. The corrosion studies using CMAS coating of the CMCs reveal that CMCs had a weight gain of ~6% owing to formation of α-Al_2O_3 at 1000 °C. The SE image indicated the penetration of CMAS into the porous CMC. At 1000 °C, CMAS degraded to form a black glassy substance (Calcium alumino silicate) with traces of Mg which led to corrosion of the matrix. Indentation fracture toughness of the oxide/oxide CMCs was 7.78 ± 0.5 MPa $m^{0.5}$ which degraded by ~12% at 1000 °C after 10 h in the presence of CMAS. A mathematical model derived through diffusion equation indicated weight gain of ~0.3 g which was closer to experimental data.

1. Introduction

Ceramic matrix composites (CMCs) are being demonstrated as promising candidates in the gas-turbine and hot-section components as alternatives for superalloys due to their lower density, chemical stability and excellent mechanical properties at high temperatures [1,2]. Even with these promising properties, CMCs are susceptible to corrosion through water vapour and CMAS (Calcium-magnesium aluminosilicate) environments at high temperatures. For instance, SiC/SiC composites undergo rapid recession due to formation of $Si(OH)_4$ in a water vapour environment [3,4]. Thus, to protect CMCs from the recession behaviour, protective coatings such as Environmental Barrier Coatings (EBCs) are utilised to protect the gas-turbine (GT) engines for aircraft propulsion, power generation and marine propulsion [5,6]. For GT and hot-section components, one of the fundamental properties is to have a good resistance towards hot corrosion as well as molten CMAS at higher temperatures in different environments [7,8].

CMAS attack occurs when atmospheric dust including sand, volcanic ash and other silica particles are being deposited on the surface of turbine blades. These deposited particles melt and wick into the columns of coatings/turbines leading to cracks and spallation [9,10]. Various attempts have been made to mitigate the CMAS attacks in thermal/-environmental barrier coatings (T/EBCs) in the past few decades [5,11,12]. One such approach is to utilise the de-wetting of the outer layer. However, during thermal cycling and operation these outer layers cracked or eroded. Other approaches such as involving sacrificial layers or crystalline Al_2O_3 reinforcements in barrier coatings have been attempted to arrest the CMAS propagation [13]. These approaches provided limited success but due to mismatch between barrier layers and Al_2O_3, there was a continuous detrimental effect during thermal cycles [14]. Likewise, various TBC and EBC materials have been studied for CMAS attack on CMCs to understand the substrates recession behaviour [15,16]. Research on SiC/SiC composites are well established and its corrosion as well as mechanical behaviour has been extensively studied [3,17]. However, there has been limited study on its counterpart oxide-oxide CMCs under similar conditions [18,19].

Hence, this paper focuses on understanding the effect of CMAS on the oxide/oxide CMCs (AS-N610) at different temperatures (800 °C, 900 °C & 1000 °C) for different intervals of time (1, 5 & 10 h). The CMAS coating was applied onto the oxide CMCs at room temperature and hot

* Corresponding author.
** Corresponding author.
E-mail addresses: K1825123@kingston.ac.uk (K. Ramachandran), k1803433@kingston.ac.uk (B. Chaffey), k1546465@kingston.ac.uk (C. Zuccarini), J.Bear@kingston.ac.uk (J.C. Bear), d.daniel@kingston.ac.uk (D.D. Jayaseelan).

https://doi.org/10.1016/j.ceramint.2022.09.294
Received 4 August 2022; Received in revised form 5 September 2022; Accepted 22 September 2022
Available online 26 September 2022

condition (250 °C). The hot substrate condition is to mimic the effect of CMAS on a hot blade while in contact. This could allow us to understand the effect of CMAS in real time.

2. Experimental details

2.1. Materials

Commercially available oxide/oxide CMCs designated as AS-N610 were procured from Ansaldo Energia, Italy in the form of 300 × 300 × 3 mm plates. These CMCs were manufactured by COI ceramics, CA using infiltration of matrix precursors of aluminosilicate by sol-gel techniques followed by vacuum bagging technique along with pressureless sintering. The required samples for the study with dimension 10 × 10 × 3 mm were cut using waterjet cutting (Custom waterjet cutting Ltd., Uxbridge, UK). Further material description and properties of the oxide-oxide CMC are available in our previous study [18]. The other powders for the study included calcium oxide, magnesium oxide, aluminium oxide, and silicon dioxide which were obtained from Fishers Scientific Pvt. Ltd, UK with a purity range of ~98% and average particle size of 70 μm.

2.2. CMAS preparation

The composition of CMAS is similar to previously used by Drexler *et al.* and Kramer *et al.* [11,12]. The CMAS mixture consisted of 37.1 wt% CaO, 3.5 wt% MgO, 7.1 wt% Al_2O_3 and 52.3 wt%. SiO_2 was mixed with ethanol in the ratio of 1:2 and wet ball milled (Planetary ball milling, Retsch, Germany) at 300 rpm for 4 hr with resting time of 5 min every half hour. The wet ball milled CMAS slurry was heated at 1200 °C for 4 hr. The resultant powder was crushed using mortar/pestle and screened using a #500 mesh sieve.

2.3. CMAS coating

The synthesised CMAS powder was mixed with ethanol at a ratio of 2:1 to form a thick and sprayable slurry. The slurry was loaded into a hand-held atmospheric spray gun (Silverline, United Kingdom) with nozzle diameter of 1 mm and sprayed it over oxide/oxide CMC substrates. The coating was carried out at two different substrate conditions - (1) room temperature and (2) substrate heated at 250 °C for 2 h using a box furnace (Carbolite Gero Ltd, United Kingdom). The coated substrates were dried at room temperature for 24 hr and further dried at 200 °C for 2 hr with a slow heating rate of 1 °C/min.

2.4. Characterisation & testing methods

Heat treatments of the CMAS coated oxide/oxide CMCs were carried out to understand the effect of CMAS attack at different temperatures (800 °C, 900 °C & 1000 °C) and time intervals (1 hr, 5 hr & 10 hr). For corrosion studies, samples were placed in an alumina boat at a wedged angle to minimise the direct contact between the alumina boat and substrates. Fig. 1 shows the temperature profile of the corrosion experiment. All samples were heated to desired temperature at a heating rate of 120 °C/h and held for different intervals of time and cooled down to room temperature at a cooling rate of 120 °C/h. The surface of oxide/oxide CMCs, corrosion tested samples and CMAS powder were characterised using Scanning Electron Microscopy (Zeiss SM350D, Kingston University) fitted with Energy-Dispersive X-ray spectrometer (EDS). X-Ray diffraction (XRD) technique was used to identify the phases of the synthesised CMAS powder and corroded oxide CMCs. XRD was carried out with 2θ values ranging from 0 to 90° with a step rate of 0.1° sec^{-1}. Vickers hardness of the oxide CMCs and coated CMAS substrates were evaluated as per ASTM C1327 with indentation load of 10 N and dwell time of 20 s. The diagonals of the cracks were measured to calculate the indentation fracture toughness as per previous studies using Evans and Charles equations [20,21].

3. Results & discussion

3.1. Characterisation of CMAS & oxide CMCs

Fig. 2 shows the SE images of oxide/oxide CMCs. Fig. 2(a) reveals that the oxide/oxide CMC has a typical 0°/90° fibre orientation on the surfaces with Nextel™ 610 fibres continuously woven in the aluminosilicate matrix. At higher magnification, the matrix shows the presence of sub-micron sized α-alumina grains on the surface (Fig. 2(b)). Fig. 2(c) shows the fibres at higher magnification showing an undamaged surface. The elemental compositions carried out at different localized areas namely A, B, C and D in Fig. 2(a) are given in Table 1. It is inferred from EDS analysis that the substrate contained only three elements i.e., oxygen, aluminium, and silicon. The higher percentage of aluminium and oxygen indicates presence of aluminium oxide on the CMCs. The small traces of silicon on the EDS indicates presence of aluminosilicate matrix.

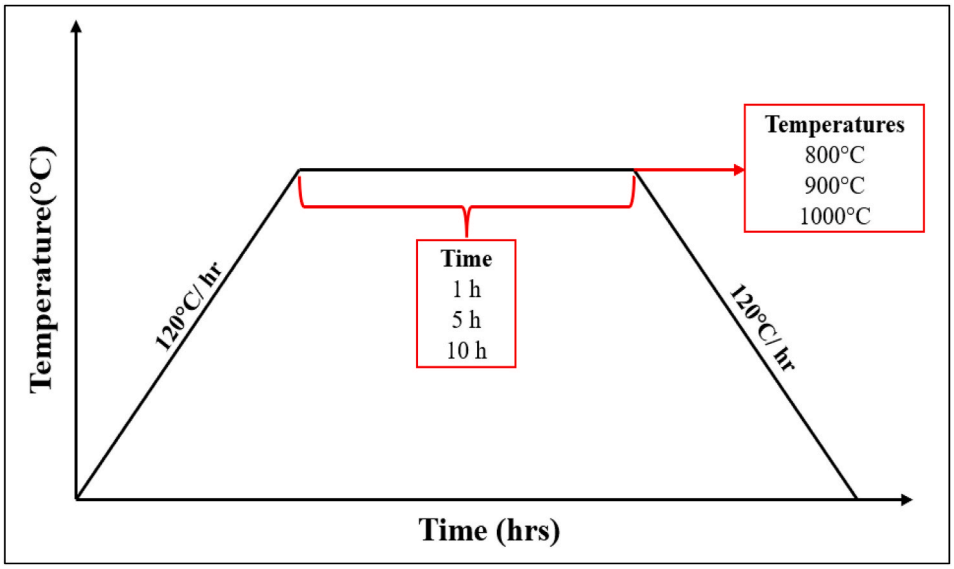

Fig. 1. Temperature Profile of Corrosion studies on oxide-oxide CMCs.

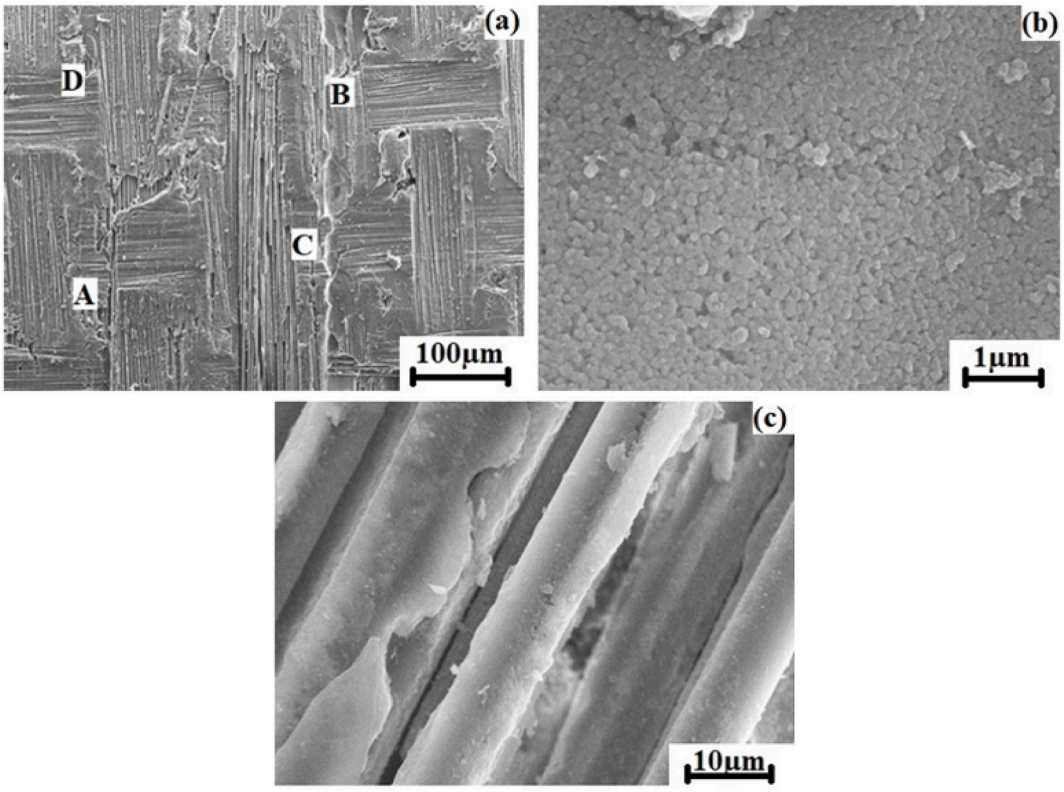

Fig. 2. SE images of Oxide CMC (AS-N610) (a) Fiber Orientation (b) alpha alumina on surfaces and (c) NextelTM610 fibers on CMC.

Table 1
Elemental distribution of oxide CMC (AS-N610) at different localized zones.

Elements / Localized Zone	O (Wt.%)	Al (Wt.%)	Si (Wt.%)	Total (Wt.%)
Spectrum A	50.2	43.12	6.68	100
Spectrum B	50.37	43.16	6.47	100
Spectrum C	50.15	43.5	6.35	100
Spectrum D	49.15	44.26	6.6	100

The XRD patterns of oxide CMCs and synthesised CMAS powder are given in Fig. 3. The peaks of oxide CMCs include corundum and mullite ($3Al_2O_3$:$2SiO_2$). The higher amount of corundum peaks is attributed to alumina contribution from matrix and fibres. The XRD of CMAS (Fig. 3) reveals the peaks of anorthite ($CaAl_2Si_2O_8$), corundum (α-Al_2O_3) and diopside ($MgCaSi_2O_6$). The presence of anorthite and diopside indicates a proper mixing of the powders and formation of CMAS. These observations are in good agreement with previously published data [22]. The SE image of CMAS (Fig. 4) confirms the homogeneous mixing of powders through the ball milling process. EDS analysis was carried out in a few different places numbered in the SE image in Fig. 4 and the elemental compositions are tabulated in Table 2.

3.2. Effect of CMAS

The CMAS coated oxide/oxide CMC substrates were heated at temperatures of 800 °C, 900 °C and 1000 °C for different time intervals (1, 5 & 10 h) to understand the effect of corrosion in oxide/oxide CMCs. There is a clear weight gain in all samples after the corrosion studies and the weight gain vs heat treatment temperature is plotted in Fig. 5. It is evident that the CMAS coated on the hot substrate had higher weight gain compared to the CMAS coated on cold substrate. The weight gain of the hot substrates was observed to be ~3–6% higher than the cold substrates. This increase in the weight could be due to the adherence of the CMAS onto the hot substrate due to the quick evaporation of the OH^- molecules which allows more CMAS to deposit on the surfaces. However, the weight gain of some cold coated substrate at 900 °C and 1000 °C might be owing to the melting of the glassy CMAS which has a transition glass temperature of above 800 °C which could form different oxides on surfaces. The changes in weight gain in most of the coated samples were in second decimal in most cases inferring that the oxide layers formed were limited owing to pre-occurring oxide structure in the CMAS and substrates.

Fig. 6 shows the XRD of the cross-sectional surface of a CMAS coated sample after being heated for 10 h at different temperatures in two different conditions. The peaks at 800 °C showed the presence of mullite with a trace of anorthite. The presence of anorthite peak in the XRD supports the penetration of the CMAS into the substrate at 800 °C. However, anorthite peak diminishes with increase in temperature showing the diffusion of anorthite to α-Al_2O_3 and SiO_2 at high temperature. Most of the peaks corresponded to α-Al_2O_3 in all three temperatures. Few peaks correspond to mullite ($3Al_2O_3$:$2SiO_2$). The increase in the α-Al_2O_3 peaks could have been due to the lower Gibbs activation energy of α-Al_2O_3 compared to SiO_2. Thus, formation of α-Al_2O_3 is comparatively faster in atmospheric conditions resulting in still the presence of alumina peaks at all the temperatures [23]. This could have been the case for both hot coated and room temperature conditions as most peaks (Fig. 6 (Right)) also showcased a high amount of α-Al_2O_3. Comparing with the RT coated substrates, it could be assumed that owing to adherence of the CMAS and further diffusion during corrosion studies, the intensity of α- Al_2O_3 peaks formed at hot coated substrates was higher than the other set. The presence of mullite peaks is from the matrix. The presence of mullite and α-Al_2O_3 peaks at 1000 °C supports the thermal stability of oxide CMCs not being corroded by CMAS.

The stability of oxide CMC has also been confirmed by EDS analysis given in Table 3 where most elements present in the EDS still correspond to CMAS and oxide substrate. Although EDS indicated the change in the elemental composition with high amounts of Al and O elements followed

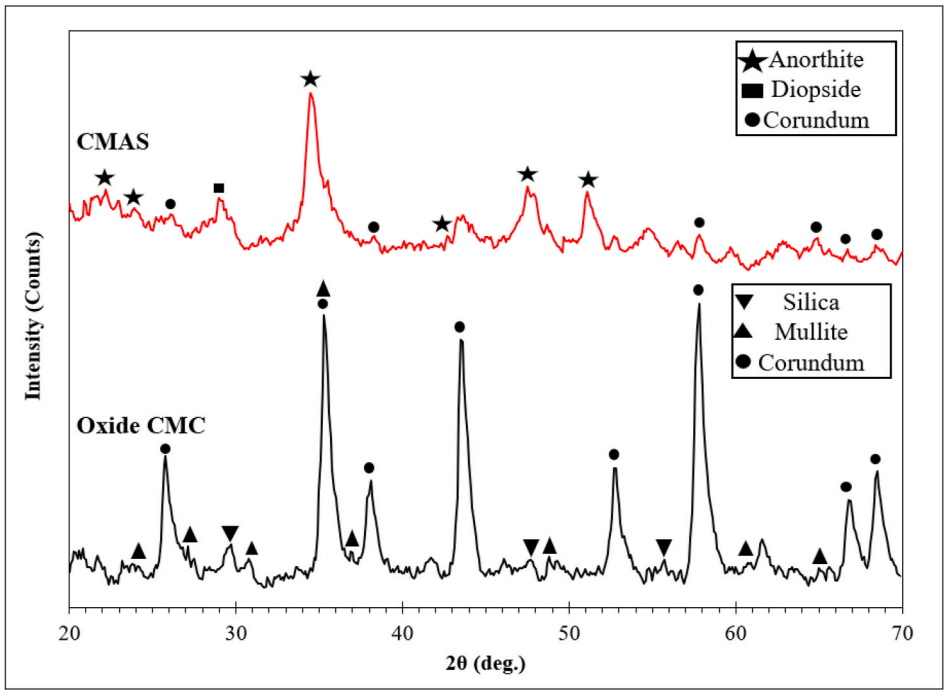

Fig. 3. XRD pattern of the oxide CMC substrate and CMAS powder.

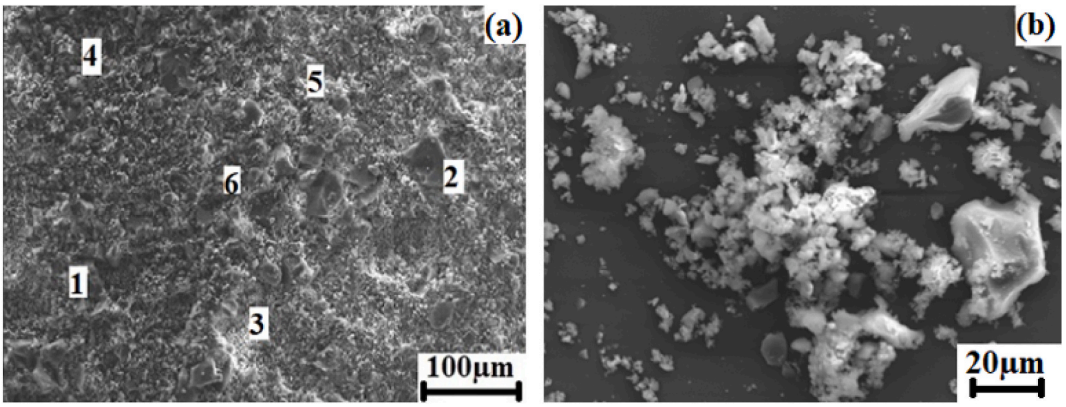

Fig. 4. SE images of synthesised CMAS powders at (a) low magnification with EDS spectrums and (b) higher magnification.

Table 2
EDS of synthesised CMAS powder attained at different spectrums.

Elements / Spectrum	O (Wt.%)	Mg (Wt.%)	Al (Wt.%)	Si (Wt.%)	Ca (Wt.%)
Spectrum 1	57.61	2.36	2.46	21.34	16.22
Spectrum 2	59.5	2.29	1.01	20.24	15.46
Spectrum 3	58.26	2.28	2.44	17.15	18.88
Spectrum 4	57.84	2.3	1.44	17.86	18.56
Spectrum 5	59.52	1.92	1.21	22.09	15
Spectrum 6	63.69	1.87	0.99	21.71	10.73

by Si, the increase in Al and O in Table 3 indicates the formation of Al_2O_3 on the surfaces of the substrate which could have been diffused from CMAS. The presence of the Al, O and Si elements even after the CMAS corrosion shows the stability of oxide CMCs. Previous study shows the thermal shock resistance of oxide CMC at temperature of 1200 °C [18]. The amount of Ca diminished with increase in temperature which supports the penetration of CMAS into the matrix along with the diffusion of anorthite. However, XRD does not pick up any peaks of Ca or Mg other than anorthite peak at 800 °C. This could have been due to the low elemental percentage of Mg and Ca or melting of the CMAS in the porous matrix which could have hidden the traces of Ca and Mg. With increase in the temperature, Mg peaks diminished (<0.5 wt%) for samples at 1000 °C. This might be due to diffusion of MgO into the porous areas of the substrate between the temperature range 800 °C–1000 °C [24].

Fig. 7 represents the cross-sectional SE images of CMAS coated oxide samples after corrosion at different conditions. SE images showed clear deposition of CMAS on the fiber surfaces and it has been confirmed with EDS in Table 3. The traces of CMAS on fiber surfaces proves the CMAS penetration in porous oxide matrix. Although penetration of the CMAS has been confirmed by SEM in the substrates, microstructural observation indicated no corrosion along the substrate. Likewise, no identifiable CMAS layers were found on the top surfaces of substrates showcasing the melting of CMAS layer and further penetration onto the porous oxide matrix even at temperature range of 900 °C. The penetration of CMAS into the porous matrix was confirmed in the EDS (Table 3) where presence of Mg, Ca, Al and Mg were determined in the cross-sectional surface analysis.

On the other hand, Fig. 8(a) & (b) represents the cross sectional SE of

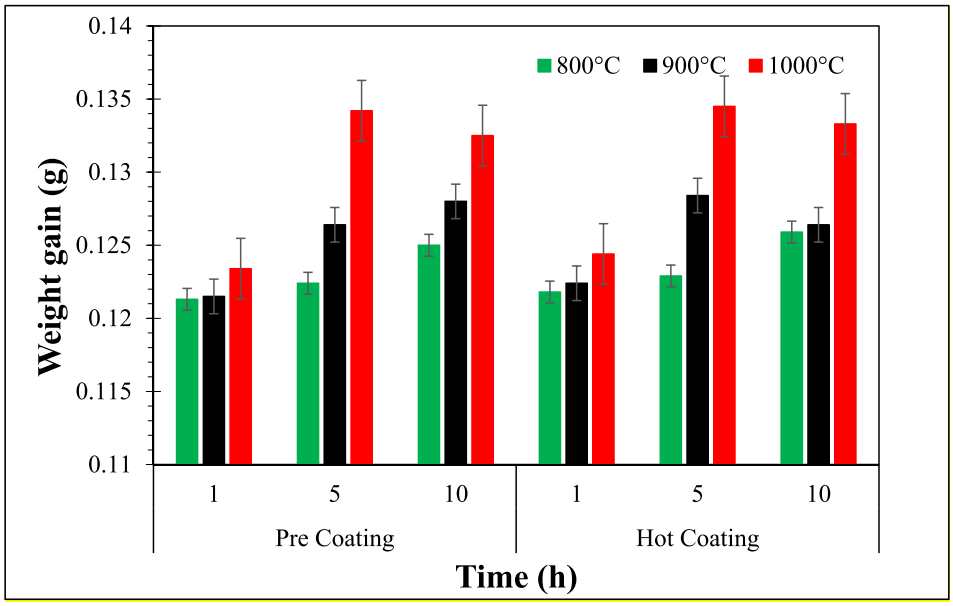

Fig. 5. Weight gain of pre-coated and hot-coated CMAS substrate after different corrosion time.

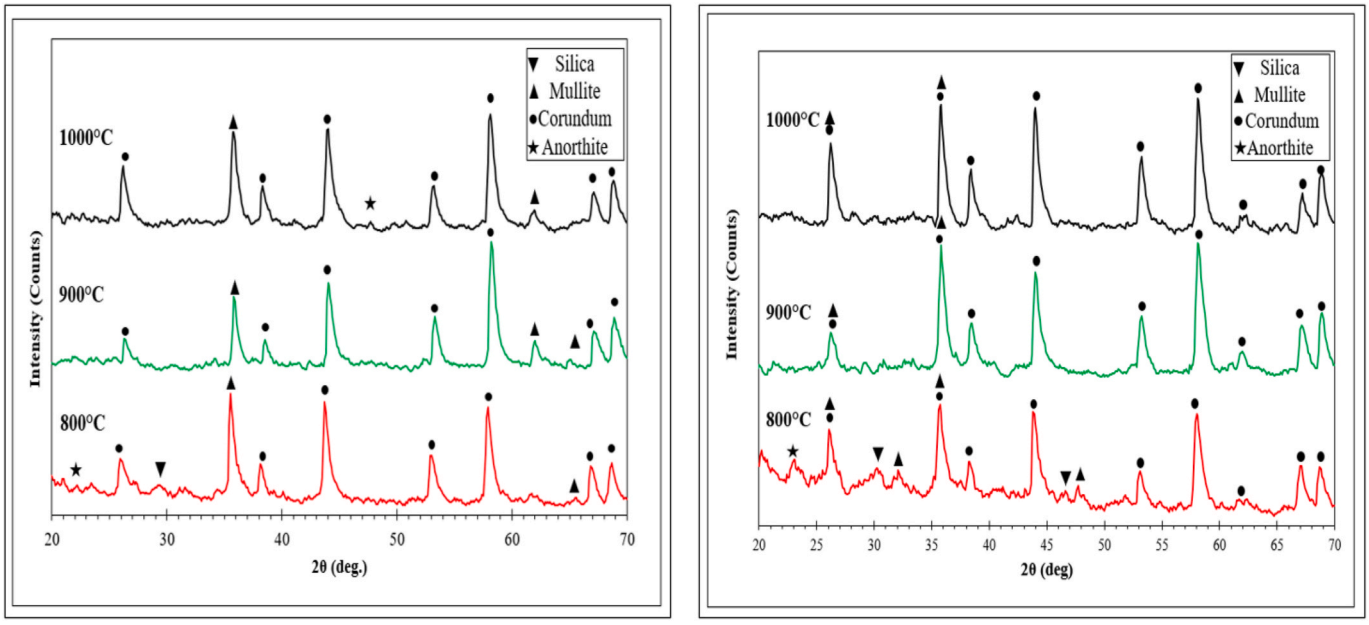

Fig. 6. After corrosion cross-sectional XRD phases of CMAS coated RT substrate (left) and hot coated substrate (right) for 10 h.

Table 3
Elemental distribution of room temperature and hot coated substrate after corrosion study at 10 h at different temperature.

Temperature	Type of Coating	Elements / Location	O (Wt.%)	Mg (Wt.%)	Al (Wt.%)	Si (Wt.%)	Ca (Wt.%)
800 °C	RT	Spectrum A	53.55	1.36	13.29	16.34	14.26
		Spectrum B	48.34	0.75	15.4	14.95	18.56
900 °C		Spectrum 1	62.18	0.93	9.4	17.15	10.2
		Spectrum 2	59.94	0.54	18.3	12.86	6.21
1000 °C		Spectrum A	60.26	0.24	21.45	10.81	4.24
		Spectrum B	58.21	0.34	28.06	10.29	1.7
800 °C	Hot Coating	Spectrum 1	56.52	0.98	10.21	15.09	14.55
		Spectrum 2	63.27	1.87	4.62	16.72	11.49
900 °C		Spectrum 1	62.38	1.02	6.27	15.79	11.2
		Spectrum 2	58.63	1.05	7.35	21.48	10.73

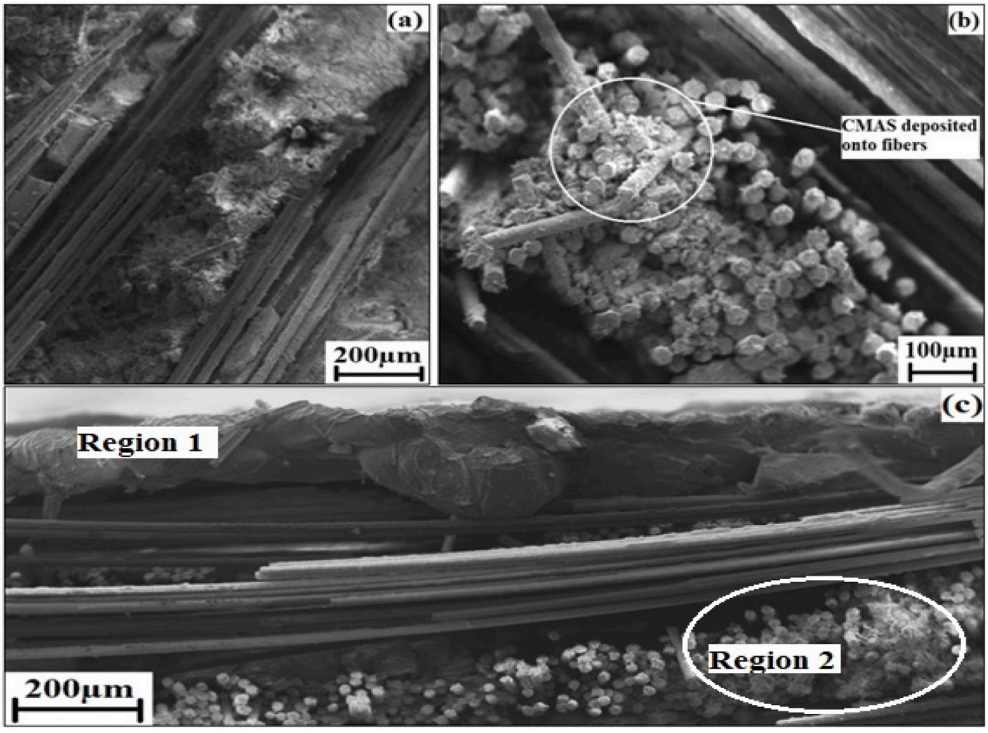

Fig. 7. (a) Cross section SE of substrate near coated area (5 h/800 °C RT), (b) 5 h/800 °C Hot Coated substrate after corrosion and (c) view of the substrate near coated region (10 h/900 °C RT).

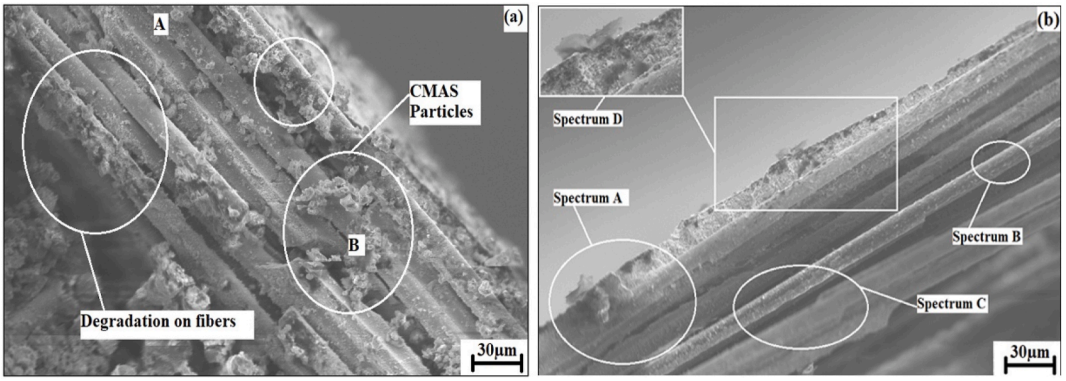

Fig. 8. Cross sectional SE image of corroded substrates at 1000 °C/10 h for (a) RT coated and (b) Hot coated.

CMAS coated samples corroded at 1000 °C. Fig. 8(a) shows the degradation of the matrix due to the attack of CMAS on the surfaces. Fig. 8(a) also shows visibility of traces of molten CMAS on the surfaces of the oxide matrix which confirms the penetration of the CMAS onto the porous matrix. The non-visibility of the CMAS layers on the surfaces of oxide substrate might be due to the higher porosity percentage in the substrate along with high amount of open channels with prevailing pores, cavities and microcracks which could accelerate the infiltration of molten CMAS into the substrate [25]. The dark spots observed in Fig. 8 (b) on the matrix of oxide substrates is the formation of a thin glassy phase at 1200 °C for 10 h in air. EDS (Table 4) carried out on black glassy surface reveals it to be CAS (calcium aluminosilicate) with small traces of Mg as reported in Table 4 [25]. The closer observation of the SE image showed that the matrix was eaten away slowly by the black glassy substance. This was also the case for fibers which show some corrosion at high temperatures. With increase in temperature, CMAS eat away or degrade the oxide matrix as well as fibers leading to damage drop in the mechanical due to the infiltration of the CMAS onto the entire matrix.

Table 4
EDS of hot substrate coated CMAS after corrosion test at 1000 °C for 10 h.

Elements / Localized Zone	O (Wt. %)	Al (Wt. %)	Mg (Wt.%)	Si (Wt. %)	Ca (Wt. %)	Total (Wt.%)
Spectrum A	60. 62	21.64	0.30	14.42	3.02	100
Spectrum B	64.26	24.95	–	10.79	–	100
Spectrum C	56.46	28.41	0.14	14.96	–	100
Spectrum D	28.97	44.47	0.22	21.69	4.65	100

3.3. Effect of CMAS on fracture toughness

Indentation fracture toughness was measured for oxide CMC prior and after CMAS corrosion to identify the effect of CMAS onto the substrate. The substrate had a fracture toughness of 7.78 ± 0.5 MPa $m^{0.5}$ at room temperature. The strength of the oxide CMC was closer to values reported by other researchers [26,27]. However, with CMAS it was

indicated that the fracture toughness reduced as represented in Fig. 9. Fig. 9 indicates the effect of CMAS corrosion on oxide CMC after 10 h. The samples coated with CMAS in RT show a reduction of ~4% for 800 °C, ~7% for 900 °C and ~10% for 1000 °C whereas hot coated CMAS shows high reduction in values compared to RT. Hot coated samples showed ~7% loss for 800 °C, ~10% for 900 °C and ~13% for 1000 °C which was over ~3% increase than the RT samples.

The deterioration on fracture toughness at CMAS coated samples could have been due to the temperature and further infiltration of CMAS into the substrate at high temperature which degrades the matrix and fibers. Choi *et al.* reported the degradation in the mechanical properties of Nextel™720/alumina CMC with CMAS infiltration due to the direct brittle fracture with no visible fiber pull-outs [26]. However, SE images indicated no visible fractures due to the CMAS infiltration. However, degradation on the matrix and fiber could make the CMCs brittle leading to reduction in mechanical properties with increase in temperature and CMAS infiltration. Further, pre-heating of oxide CMCs shows higher reduction in fracture toughness compared to RT coated CMAS which might be attributed to the pre-heating of substrate at 250 °C. The coating of CMAS enhanced the brittle behaviour which could be supported by the high intensity peaks of α-Al_2O_3 present in the XRD. The SE images (Fig. 7) of CMAS coated oxide CMC samples show no pull-out mechanisms or any kind of cracks in the matrix. This infers that the CMAS which penetrates the porous oxide matrix could have degraded the matrix as well as fiber leading to reduction in mechanical properties [26].

3.4. Corrosion rate modelling

The corrosion model for the oxide CMCs was developed by considering the factor that the corrosion is induced by the parabolic oxidation of material. Using the law of Lavoisier, the first assumption is made that nothing can be created or destroyed, hence there is no flow divergence [23].

$$\frac{\partial \rho}{\partial t} + \nabla \cdot J = 0 \tag{1}$$

Where ρ is the flow density position vector ($\vec{r}$) and J is flux of substance. Further, in a continuum regime, total flux is defined as the rate of change of concentration or concentration gradients. Hence:

$$J = -D\nabla\rho \tag{2}$$

where D denotes the diffusion constant which depends on the material. Taking divergence of Eq (2) and combining with (1) leads to diffusion equation in second order position and first order in time.

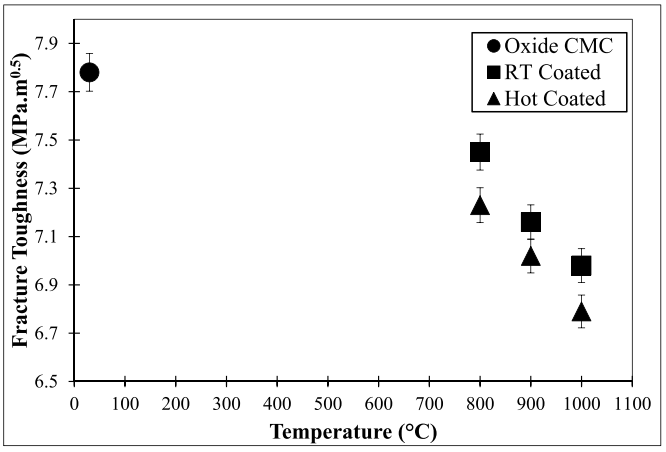

Fig. 9. Effect of CMAS on fracture toughness of the oxide CMCs.

$$\frac{\partial \rho}{\partial t} - D\nabla^2\rho = 0 \tag{3}$$

This partial differential equation will have a time dependent part that will be function of exponential and position dependent part which will be sinusoidal.

$$\rho(r,t) = e^{At}\cdot[B\sin D_r(x,y,z,t) + C\cos D_r(x,y,z,t)\,] \tag{4}$$

In Eq (4), A, B and C are arbitrary constants and D is diffusion constant which depends on the material. The model is based upon the assumption that corrosion is induced solely by oxidation with such variable increasing only in one direction as per Deal-Grove modelling. The vectorial problem of equation (3) an (4) is therefore simplified to a one-dimensional equation by disregarding volume thickness. Hence, the rate of density change (4) can be written as:

$$\rho(x,t) = e^{At}\cdot[B\sin Dx + C\cos Dx] \tag{5}$$

Assuming the change in concentration leads to corrosion. Then solving Eq (5) would allow us to determine the function that could support the rate of change of material density induced by corrosion. The boundary conditions to attain the density function are attained by solving the arbitrary constants. First assumption is to showcase that total density is equivalent to density of sample (ρ_m). Therefore, substituting the values in Eq (5)

$$\rho(0,0) = \rho_{\mathrm{m}} \tag{6}$$

$$e^{A\cdot 0}\cdot[B\sin D\cdot 0 + C\cos D\cdot 0\,] = \rho_{\mathrm{m}} \tag{7}$$

$$C = \rho_{\mathrm{m}} \tag{8}$$

The second assumption will be rate of change in density is consistent with change of density induced by corrosion/oxidation (ρ_o) in the material. Therefore, first derivative is set equal to T. Let

$$[B\sin Dx + C\cos Dx\,] = F(x) \tag{9}$$

Then substituting its value in Eq (5) and deriving it could lead to

$$\rho(x,t) = e^{At}\cdot F(x) \tag{10}$$

$$\frac{\partial \rho}{\partial t} = A\cdot e^{At}\cdot F(x) \tag{11}$$

$$\frac{\partial \rho}{\partial t}(0,0) = \rho_{\mathrm{o}} \tag{12}$$

Evaluating Eq (12) with respect to Eq (5) by setting to 0 with respect to T yields:

$$A = \frac{\rho_{\mathrm{o}}}{\rho_m} \tag{13}$$

Final assumptions will be that the rate of density change in the material will remain constant over time could form Eq (14) and evaluating to Eq (5) yields

$$\frac{\partial \rho}{\partial x}(0,0) = 0 \tag{14}$$

$$B = 0 \tag{15}$$

Based upon the assumptions made, it is expected that due to oxygen diffusion the density is described by the following equation.

$$\rho(x,t) = \rho_m e^{\frac{\rho_{\mathrm{o}}}{\rho_m}t}\cos D\,x \tag{16}$$

Equation (16) describes a particular solution on how density changes as a function of position and time. As Corrosion rates are described

either by weight loss(gain) or by depth of penetration and, given that the ultimate goal of this model is to find a formula that estimates the weight lost or gained as a result of corrosion, there is the need to introduce the general rate of corrosion equation. This is given by:

$$R = \frac{kW}{\rho A t} \tag{17}$$

Where k is a constant that depends on the material diffusivity, ρ the environmental density, A the area of the sample and W the weight loss/gain due to corrosion. Equation (17) is not time dependant, however the initial assumption is that the rate of change of density is equal to the rate of carrion, therefore, at constant oxidation and in an uniform corrosion attack, R is given, as a function of time as:

$$R \to R(t) = \frac{d\rho}{dt} \tag{18}$$

Differentiating equation (16) with respect to t and considering the x-part as constant yields to:

$$\frac{d\rho}{dt} = \rho_m e^{\frac{\rho_o}{\rho_m} t} \times \frac{\rho_o}{\rho_m} \times \cos Dx = \rho_o e^{\frac{\rho_o}{\rho_m} t} \times \cos Dx \tag{19}$$

Hence, combination of Eqs (17) and (19) leads to:

$$\frac{kW}{\rho A t} = \rho_o e^{\frac{\rho_o}{\rho_m} t} \cdot cosDx \tag{20}$$

Re-arranging the weight loss can be estimated as a function of time.

$$W(t) = \frac{\rho_o e^{\frac{\rho_o}{\rho_m} t} \cdot cosDx \cdot \rho A t}{k} \tag{21}$$

Equation (21) shows that the weight gained due to oxidation-induced corrosion which depends on material properties (thermal conductivity (k) and diffusivity (D) and densities (ρ_o,ρ_m), sample dimensions (area (A) and length (x)) and environmental factor (ρ) that in turns depends upon the Temperature. Assuming the parameters in Table 5 for 1000 °C it was noted that the weight gain was up to ~0.25 g, this was closer to the weight gain reported by the experiment (~0.1325 g). The difference is due to the fact that only oxidation induced corrosion has been estimated with this model and loss of material is not being considered. However, the mathematical model was successful in showcasing that such corrosion induced a weight gain. Further development by combining the density function model with the Euler Lagrange Equation [31] would lead to an optimised and more accurate model to Ref. [28] predict change in the sample due to corrosion.

4. Conclusion

Corrosion behaviour of oxide CMCs (AS-N610) coated with synthesised CMAS through atmospheric spray technique under two different substrate conditions were studied using different characterisation techniques. The substrates showed a second order weight gain (3–6%) after corrosion experiment at different temperatures and holding times owing to the molten CMAS penetrating the oxide substrate. The XRD technique reveals that after corrosion studies alumina and mullite were present as dominant phases along with small traces of CMAS constituents which indicates the stability of oxide CMCs at high temperature of 1000 °C. The presence of black glassy spots which was confirmed to be CAS was observed in samples heated at temperature 900 °C and 1000 °C. The presence of CAS with small traces of Mg on matrix and fibers ate away the matrix and fibers on the substrate with prolonged time. The black glass spots showed the degradation of the matrix at 1000 °C. Further, the fracture toughness of the CMAS oxide CMC deteriorated with increase in the temperature up to 12% for 1000 °C. An analytical model established by combining the diffusion equation and assuming the rate of oxidation induced corrosion is equivalent to the rate of change of density can lead to derivation of an equation describing weight gain/loss as a function of time. The derived equation using the model gives a weight gain of ~0.3 g which was close to the experimental values.

Table 5
Model Parameters utilised in analytical equation.

Parameter	Value	Unit
CMAS Density (ρ_m)	2830	kg/m^3
Substrate Density (ρ_o)	2930	kg/m^3
Length (L)	0.005	m
Width (x)	0.003	m
Height (H)	0.005	m
Environmental Density	0.2272	kg/m^3
Area (Lx)	0.000015	m^2
Thermal Conductivity (k)	2	W/mK
Thermal Diffusivity (D)	4.1×10^{-7}	m^2/s

Data availability

Data will be made available upon request.

Declaration of competing interest

The authors declare that they have no known competing financial interests or personal relationships that could have appeared to influence the work reported in this paper.

Acknowledgement

Authors K Ramachandran and C Zuccarini would like to acknowledge Kingston University for support towards their PhD research. Author Karthikeyan Ramachandran would also acknowledge the support from Prof. Peter Foot and Senior Technicians in Kingston University namely Mr. Dean Wells, Mr. Simon Crust, and Mr. Richard Gidden for their support in experimental and characterisation procedures.

References

[1] L. Sun, Y. Luo, Z. Tian, X. Ren, J. Li, W. Hu, J. Zhang, J. Wang, High temperature corrosion of (Er0.25Tm0.25Yb0.25Lu0.25)2Si2O7 environmental barrier coating material subjected to water vapor and molten calcium–magnesium–aluminosilicate (CMAS), Corrosion Sci. 175 (2020), 108881.
[2] J.C. Williams, E.A.S. Jr, Progress in structural materials for aerospace systems, Acta Mater. 51 (19) (2003) 5775–5799.
[3] N.A. Nasiri, N. Patra, N. Ni, D.D. Jayaseelan, W.E. Lee, Oxidation behaviour of SiC/SiC ceramic matrix composites in air, J. Eur. Ceram. Soc. 36 (14) (2016) 3293–3302.
[4] N.A. Nasiri, N. Patra, D.D. Jayaseelan, W. Lee, Water vapour corrosion of rare earth monosilicates for environmental barrier coating application, Ceram. Int. 43 (10) (2017) 7393–7400.
[5] A. Aygun, A.L. Vasiliev, N.P. Padture, X. Ma, Novel thermal barrier coatings that are resistant to high-temperature attack by glassy deposits, Acta Mater. 55 (20) (2007) 6734–6745.
[6] D.D. Jayaseelan, Y. Xin, L. Vandeperre, P. Brown, W. Lee, Development of multi-layered thermal protection system (TPS) for aerospace applications, Compos. B Eng. 79 (2015) 392–405.
[7] C.G. Levi, J.W. Hutchinson, M.H. Vidal-Setif, C.A. Johnson, Environmental degradation of thermal-barrier coatings by molten deposits, MRS Bull. 37 (2012) 932–941.
[8] V. Wiesner, B. Harder, N. Bansal, High-temperature interactions of desert sand CMAS glass with yttrium disilicate environmental barrier coating material, Ceram. Int. 44 (18) (2018) 22738–22743.
[9] R. Wellman, G. Whitman, J. Nicholls, CMAS corrosion of EB PVD TBCs: identifying the minimum level to initiate damage, Int. J. Refract. Metals Hard Mater. 28 (1) (2010) 124–132.
[10] J.G. Thakare, C. Pandey, M. Mahapatrea, R. Mulik, Thermal barrier coatings—a state of the art review, Met. Mater. Int. 27 (2021) 1947–1968.
[11] J.M. Drexler, A.L. Ortiz, N.P. Padture, Composition effects of thermal barrier coating ceramics on their interaction with molten Ca–Mg–Al–silicate (CMAS) glass, Acta Mater. 60 (15) (2012) 5437–5447.
[12] S. Kramer, J. Yang, C.G. Levi, Thermochemcial interaction of thermal barrier coatings with molten CaO-MgO-Al_2O_3-SiO_2 (CMAS) deposits, J. Am. Ceram. Soc. 89 (10) (2006) 3167–3175.
[13] V. Kumar, K. Balasubramanian, Progress update on failure mechanisms of advanced thermal barrier coatings: a review, Prog. Org. Coating 90 (2016) 54–82.

[14] R. Darolia, B. Nagaraj, Method of forming a coating resistant to deposits and coating formed thereby, US Patent 6 (11 February 2002) 720, 038.
[15] J.J.G. Chavez, R. Naraparaju, P. Mechnich, K. Kelm, U. Schulz, C. Ramana, Effects of yttria content on the CMAS infiltration resistance of yttria stabilized thermal barrier coatings system, J. Mater. Sci. Technol. 43 (2020) 74–83.
[16] N.L. Ahlborg, D. Zhu, Calcium–magnesium aluminosilicate (CMAS) reactions and degradation mechanisms of advanced environmental barrier coatings, Surf. Coating. Technol. 237 (2013) 79–87.
[17] Y. Li, M. Chen, Q. Zhang, Y. Gou, P. Xiao, P. Chen, W. Zhou, X. Zhou, Microstructure and corrosion behavior of in-situ grown Y3Si2C2 coated SiC fibers exposed to air and wet-oxygen at 1400 °C, J. Eur. Ceram. Soc. 42 (8) (2022) 3427–3436.
[18] K. Ramachandran, S. Leelavinodhan, C. Antao, A. Copti, C. Mauricio, Y. Jyothi, D. D. Jayaseelan, Analysis of failure mechanisms of Oxide - oxide ceramic matrix composites, J. Eur. Ceram. Soc. 42 (4) (2022) 1626–1634.
[19] V. Kostopoulos, T.H. Loutas, A. Kontsos, G. Sotiriadis, Y.Z. Pappas, On the identification of the failure mechanisms in oxide/oxide composites using acoustic emission, NDT E Int. 36 (8) (2003) 571–580.
[20] K. Ramachandran, R. Subramani, T. Arunkumar and V. Boopalan, "Mechanical and thermal properties of spark plasma sintered Alumina-MWCNTs nanocomposites prepared via improvised colloidal route," Mater. Chem. Phys., vol. 272, no. 125034, pp. 1-9, 202.
[21] T. Arunkumar, G. Anand, R. Subbiah, R. Karthikeyan, J. Jeevahan, Effect of multiwalled carbon nanotubes on improvement of fracture toughness of spark-plasma-sintered Ytteria-stabilized Zirconia nanocomposites, J. Mater. Eng. Perform. 30 (2021) 3925–3933.
[22] C. Mikulla, R. Naraparaju, U. Schulz, F.-L. Toma, M. Barbosa, L. Steinberg, C. Leyens, Investigation of CMAS resistance of sacrificial suspension sprayed alumina topcoats on EB-PVD 7YSZ layers, J. Therm. Spray Technol. 29 (2020) 90–104.
[23] K. Ramachandran, Z. Carmine, K. Ypshida, T. Tsunoura, D.D. Jayaseelan, Experimental investigation and mathematical modelling of water vapour corrosion of Ti_3SiC_2 and Ti_2AlC ceramics and their mechanical behaviour, J. Eur. Ceram. Soc. 41 (9) (2021) 4761–4773.
[24] J. Martinelli, E. Sonder, R. Weeks, R. Zuhr, Measurement of cation diffusion in magnesium oxide by determining the Mg18O buildup produced by an electric field, Phys. Rev. B 32 (10) (1985) 6756–6763.
[25] D.C. Faucett, S.R. Choi, Strength degradation of Oxide/Oxide and SiC/SiC ceramic matrix composites in CMAS and CMAS/salt exposures, in: Proceedings of ASME Turbo Expo, 2011. Vancouver, Canada.
[26] S.R. Choi, D.C. Faucett, Combined effects of CMAS and FOD in ceramic matrix composites, in: Proceedings of ASME Turbo Expo, 2012. Copenhagen, Denmark.
[27] M. Ruggles-Wrenn, T. Kutsal, Effects of steam environment on creep behavior of Nextel™720/alumina–mullite ceramic composite at elevated temperature☆, Compos. Appl. Sci. Manuf. 41 (12) (2010) 1807–1816.
[28] Y. Wang, H. Sun, S. Fan, Y. Gu, X. Yu, A nonlocal fractional peridynamic diffusion model, Fractal and Fractional 5 (76) (2021) 1–10.